Local bond-slip behavior and mechanisms of steel fiber-UHPC matrix interface modified by nano-engineering

Local bond-slip behavior and mechanisms of steel fiber-UHPC matrix interface modified by nano-engineering

Xinyue Wang[1, 2, *], Xinkai Ma[1, 2], Ashraf Ashour[3], Linwei Li[4], Qishuai Wu[5], Liangsheng Qiu[5], Baoguo Han[5, *]

[1] *School of Civil Engineering, Tianjin University, Tianjin, 300350 China*
[2] *Key Laboratory of Coast Civil Structure Safety of the Ministry of Education, Tianjin University, Tianjin 300350 China*
[3] *Faculty of Engineering and Digital Technologies, University of Bradford, Bradford, BD7 1DP UK*
[4] *School of Materials Science and Engineering, Tianjin Chengjian University, Tianjin, 300384 China*
[5] *School of Civil Engineering, Dalian University of Technology, Dalian, 116024 China*

* Corresponding author: xinyuewang@tju.edu.cn, hanbaoguo@dlut.edu.cn

Abstract: The bond performance at the interface between steel fibers and the ultra-high-performance concrete (UHPC) matrix plays a critical role in determining the mechanical behavior of UHPC. While nano-engineering presents promising strategies to strengthen this interface, the localized bond-slip behavior of steel fibers in nano-engineered UHPC is not fully understood, owing to complex microstructural features and pronounced stress heterogeneity along the interface resulting from the fiber-matrix modulus disparity. Combining pull-out tests, microstructural characterizations, theoretical modeling, and numerical simulations, this study elucidates two distinct mechanisms responsible for bond enhancement induced by nanofillers: the interface nano-modification effect and the transition zone nano-modification effect. The relative scale between nanofillers and steel fibers governs the enrichment or dilution of nanofillers at the interface, thereby affecting the modification efficacy within the transition zone. These mechanisms collectively contribute to a notable improvement in interfacial bond strength, reaching a peak value of 11.73 MPa — exceeding all previously reported results. The derived bond-slip constitutive models, grounded in these mechanistic insights, indicate that although nano-engineering can substantially improve the strength and durability of UHPC, it also leads to a reduction in ductility.

Keywords: Ultra-high-performance concrete (UHPC); Steel fiber-UHPC matrix interface; Nano-engineering; Bond behaviors; Local bond-slip constitutive relationship

1 Introduction

From the earliest use of Roman concrete to the development of modern high-performance concretes, improving tensile strength has remained a core requirement for these materials. To overcome the inherently low tensile strength of concrete, scientists and engineers have employed various methods, with the most significant being the introduction of various reinforcing phases to enhance concrete tensile properties [1, 2]. Since the use of plant fibers (such as straw) in ancient Roman times, there have been several key technological innovations in concrete: the introduction of reinforced concrete in the late 19th century, the advent of prestressed concrete technologies in the mid-20th century, and the development of fiber-reinforced ultra-high-performance concrete in the 21st century [3]. Each introduction of a novel reinforcing phase (i.e., steel bars, prestressed steel strands, and steel fibers) has marked a significant leap in concrete technology, expanding its range of applications. However, these innovations have also introduced challenges related to interfacial bonding.

The interface between the reinforcing phase and the concrete matrix determines the effectiveness of reinforcement. A reliable interfacial bond ensures the effective transfer of stresses between the reinforcing phase and the concrete matrix, forming the basis for their overall performance [4, 5]. In concrete materials, however, the wall effect is a fundamental phenomenon that shapes the properties of the interfacial zone. It arises from the large size difference between reinforcing phases, such as aggregates or steel fibers (millimeter- to centimeter-scale), and fine cementitious particles (1-100 μm). The presence of large-size reinforcing phases disrupts the dense packing of cement particles, creating a localized region near the reinforcement (tens of micrometers) with higher porosity and lower packing density. This microstructural heterogeneity not only alters particle distribution but also affects water and ion transport, promoting preferential nucleation and growth of hydration products such as CH and ettringite. As a consequence, the interfacial zone often exhibits inferior mechanical properties relative to the surrounding concrete, which makes it a potential weak link in the overall composite structure [6-8]. The deficiency in the interface limits the full potential of the reinforcing phase. In traditional reinforced and prestressed concrete structures, methods such as roughening of the steel reinforcement surface and optimizing the mix proportions of concrete are commonly employed to enhance bond performance between steel bars and concrete. The use of ribbed steel bars, such as spiral, herringbone, or crescent-shaped configurations, can significantly increase the mechanical interlocking force between steel bars and concrete, thereby improving bond strength, with ribbed bars showing 2-6 times higher bond strength compared to smooth bars [9-11]. Additionally, optimizing the concrete mix proportions, such as increasing the cement content and incorporating mineral admixtures, introduces a greater number of cementitious particles, particularly those with smaller sizes. Under the influence of the wall effect, the presence of more particles enhances the local packing density at the interface, while the incorporation of finer particles enables multi-scale packing that further densifies the interfacial zone. These benefits lower local porosity and contribute to the formation of a denser interfacial microstructure that enhances bond performance. Moreover, a compact interfacial transition zone provides better protection for steel reinforcement against corrosion, thereby improving the long-term durability of reinforced concrete structures [12-15].

For ultra-high-performance concrete (UHPC), the enhancement of interfacial bond performance between fibers and UHPC matrix becomes more complex, largely due to the small size of the fibers. The traditional approaches for improving the interfacial bond between steel reinforcement and concrete, such as surface roughening of the reinforcement or optimizing the UHPC mix proportions, are far less effective when applied to the fiber-UHPC matrix interface. Compared to straight fibers, the use of corrugated, helical, or hooked-end fibers (similar to replacing plain steel bars with ribbed steel bars) can enhance the interfacial bond strength by approximately 26-134% [16-18]. However, non-straight fibers tend to interlock and entangle with each other during mixing, which leads to fiber clustering and poor dispersion within the UHPC matrix [19, 20]. The poor dispersion not only reduces the workability of fresh UHPC, but also diminishes the reinforcing effect of the fibers, leading to potential stress concentration and premature cracking [21, 22]. In many researches, the mechanical properties of UHPC with straight fibers are better than those with corrugated, helical, or hooked-end fibers, although the interfacial bond strength between straight fibers and UHPC matrix is lower [23, 24]. Moreover, optimizing the mix proportion (such as optimizing water-to-cement ratio and introducing supplementary cementitious materials (SCM)) can effectively modify the fiber-UHPC matrix interface, unfortunately, the enhancement effect is limited once the matrix reaches a certain strength. Existing studies have shown that introducing SCM (e.g., silica fume) increases the compressive strength of UHPC matrix from 89 MPa to 111 MPa, leading to a corresponding bond strength improvement of 1.9 MPa (168%) [25]. In contrast, further increasing the UHPC matrix strength from 112.2 MPa to 190.2 MPa through mix proportion optimization yields a comparatively modest bond strength gain of only 1.5 MPa (19.2%) [26]. The reason for these phenomena is that the diameter of steel fibers, typically ranging from 20 to 200 μm, is not substantially larger than that of cement and SCM particles [27, 28]. The small size difference limits the ability of cement and SCM particles to enhance packing density via multi-scale accumulation, a mechanism that is more effective on larger reinforcing phases, such as steel rebars. On larger surfaces, the significant size disparity and large available surface area allow finer particles to achieve higher packing density via multi-scale packing, which is less feasible on the small-diameter fiber surface. When the particle packing near the fiber surface approaches the closest packing, further densification becomes increasingly difficult. Consequently, improving the interfacial performance of fiber-UHPC systems requires alternative strategies to modify the interfacial microstructure and bond behavior.

In recent years, with advancements in nanoscience, nano-engineering technology has provided an effective method for improving the microstructure of concrete at the nanoscale, offering a fundamental bottom-up strategy for enhancing concrete performance [29, 30]. Previous studies have shown that nano-engineering can improve interfaces, such as those between aggregate and cement paste [31], aggregate and cement mortar [32], new and old concrete [33], steel and concrete [34], and FRP and concrete [35]. These improvements are achieved by enhancing the compactness of hydration products in interfacial area, reducing the Ca/Si ratio of C-S-H gels at the interface, and minimizing defects caused by internal bleeding. As a result, the chemical-physical adhesion, mechanical micro-interlocking, and friction in these interfaces are significantly enhanced [34, 35]. Moreover, the incorporation of nanofillers can also enhance the bonding performance between steel fibers and the UHPC matrix. Research has indicated that the incorporation of nano-SiO_2 [36], nano-$CaCO_3$ [37], and graphene oxide [38] can increase the bond strength between steel fiber and UHPC matrix by 1.0 MPa (35%), 1.3 MPa (45%), and 2.6 MPa (29%), respectively. This modification effect is attributed to the filling and nucleation effects, where nanofillers at the interface can fill voids and induce the generation of hydration products, thereby improving the densification of the interface and enhancing the bond strength [11]. However, the spatial distribution of nanofillers at the fiber-matrix interface remains poorly understood, yet is fundamental for achieving the aforementioned enhancement effects. In addition, nanofillers exhibit varying physical sizes, chemical compositions, and surface properties, which may result in distinct mechanisms for modifying the fiber-UHPC matrix interface. For instance, nano-SiO_2, may exhibit limited filling capability due to its ultra-fine particle size [1], while surface-inert nanofillers, such as carbon nanotubes, may not be able to exert obvious nucleation effect [39]. The modification effects and mechanisms of nanofillers with different characteristics on the steel fiber-matrix interface need further study. Finally, during the pull-out process, there is significant stress heterogeneity along the fiber matrix interface. This is due to the significant difference in elastic modulus between steel fibers and UHPC matrix, resulting in highly concentrated stress near the fiber ends, while load transmission gradually decreases along the embedded length. This uneven stress distribution plays a crucial role in controlling local bond slip behavior and overall interface performance [40, 41]. Unfortunately, current studies have mainly focused on the average interfacial bond performance of fiber-UHPC matrix interfaces modified by nano-engineering, with insufficient research on the local interfacial microstructures and constitutive bond-slip relationships.

This paper aims to investigate the local bond-slip behavior of interface between steel fiber and nano-engineered UHPC matrix, reveal the underlying modification mechanisms, as well as establish the local bond-slip relationship. For these purposes, the bond behaviors between steel fibers and nano-engineered UHPC matrix were first studied using a single fiber pull-out test, analyzing the effect of different nanofillers on the interface bond strength, slip, and failure modes. Subsequently, microstructural characterization techniques, such as scanning electron microscopy (SEM), energy dispersive spectroscopy (EDS), and backscattered electron imaging (BSE), were employed to characterize distribution of nanofillers and analyze the effects of nanofillers on the interfacial microstructures. Finally, this study combined the cohesive zone model (CZM) and finite element method (FEM) techniques to obtain the local constitutive relationship of the steel fiber-UHPC matrix interface.

2 Experimental schemes

2.1 Sample preparation

2.2.1 Raw materials and mix proportion

P·O 42.5 R Portland cement (GB175-2007, China), grade II fly ash (GB/T 1596-2017, China), and silica fume with a particle size range of 0.1-0.3 μm were used as cementitious materials to fabricate UHPC matrix. Moreover, quartz sand with a particle size of 0.12-0.83 mm was used as aggregate. Given the low water-to-binder ratio of 0.24, a polycarboxylate superplasticizer with a water reduction capacity of 30% at a dosage of 1.1 wt.% of cement was blended into UHPC to enhance the workability of fresh UHPC matrix. Moreover, 6 representative and widely used nanofillers, namely nano-SiO_2, nano-TiO_2, hydroxyl-functionalized carbon nanotubes (H-CNTs), nickel-coated carbon nanotubes (Ni@CNTs), multi-layer graphene (MLG), and nano-BN, were used to modify the interfacial bond behaviors between steel fibers and UHPC matrix. The content levels of nano-SiO_2, nano-TiO_2, H-CNTs, Ni@CNTs, MLG, and nano-BN were 2 wt.%, 3 wt.%, 0.3 wt.%, 0.3 wt.%, 0.5 wt.%, and 0.3 wt.% of cement, respectively, based on their optimal content levels on the modification of cement-based materials [1, 31]. The mix proportions of UHPC matrix in this study are listed in Table 1, while the detailed properties of raw materials can be found in Refs. [31, 32]. Steel fibers commonly used in UHPC applications with a diameter of 0.2 mm, a length of 12 mm, and a tensile strength of 1100 MPa was employed in this study. Noteworthily, to ensure consistency in the surface state, all steel fibers used in this study were obtained from the same batch and supplier, without additional surface treatment.

2.2.2 Specimen design

To investigate the effect of nanofillers on the interfacial bond behaviors between steel fibers and UHPC matrix, specimens for the pull-out test were fabricated in this study. Based on the China Standard CECS 13: 2009 [42], the embedded depth of steel fiber in a pull-out test should meet the following criteria.

$$l_{em} \leq 0.4 l_f \tag{1}$$

$$l_{em} \leq \frac{f_f d_{eq}}{f_m} \tag{2}$$

where l_{em} and l_f (=12 mm) represent the embedded depth and fiber length, respectively. f_f=(1100 MPa) and f_m (=104.24-130.55 MPa [43]) represent the tensile strength of fiber and the compressive strength of concrete, respectively. d_{eq} is the equivalent diameter of the steel fiber; in the case of cylindrical fibers, it equals its actual fiber diameter. Hence, the embedded depth of 4 mm was selected in this study. Moreover, cylindrical UHPC matrix specimens, with a diameter of 30 mm and a height of 15 mm, were used in this study to minimize the boundary effect, as shown in Fig. 1.

Table 1 Mix proportions of UHPC matrix without/with nanofillers

No.	Nanofiller	Mix proportion (mass ratio)						
		Binder			Water	Sand	Superplastizer	Nanofiller
		Cement	Fly ash	Silica fume				
1	-	1	0.25	0.313	0.375	1.375	0.011	-
2	Nano-SiO_2	0.97	0.25	0.313	0.375	1.375	0.015	0.03
3	Nano-TiO_2	0.98	0.25	0.313	0.375	1.375	0.011	0.02
4	H-CNTs	0.997	0.25	0.313	0.375	1.375	0.013	0.003
5	Ni@CNTs	0.997	0.25	0.313	0.375	1.375	0.011	0.003
6	MLG	0.995	0.25	0.313	0.375	1.375	0.011	0.005
7	Nano-BN	0.997	0.25	0.313	0.375	1.375	0.011	0.003

2.2.3 Specimen preparation

The sample preparation process included three main steps: nanofiller dispersion, mixing, as well as molding and curing, as illustrated in Fig. 1. The detailed preparation procedure is outlined as follows: (1) Nanofiller dispersion: For non-carbon nanofillers, such as nano-SiO_2, nano-TiO_2, and nano-BN, dispersion was achieved in water via using the superplasticizer as dispersing agent and stirring at low speed for 60 s; For carbon nanofillers, including H-CNTs, Ni@CNTs, and MLG, their uniformly distributed suspensions were prepared with the aid of ultrasonication for 600 s, employing the superplasticizer as the dispersing agent. (2) Mixing: The nanofiller suspension was mixed with silica fume and stirred at low speed for 60 s. Then, cement and fly ash were added to the mixture, followed by stirring at both low and high speeds for 120 s. Finally, sand was added to the mixture and stirred at low speed for 60 s, followed by high-speed stirring for 240 s. (3) Molding and Curing: The well-mixed fresh UHPC matrix was poured into oiled molds with a diameter of 30 mm and a height of 15 mm, followed by vibration for 60 s. Steel fibers were then inserted vertically into the fresh UHPC matrix, with the aid of a PVC board to ensure they were embedded in the desired position. Afterward, the samples and molds were cured at a standard curing condition, i.e., a temperature of 20±2°C and a relative humidity over 95%, for 24 h before demolding. Finally, the demolded specimens were submerged in water at room temperature for 28 d before testing.

Noteworthily, due to the inherent variability in single-fiber pullout tests, 12 samples were prepared for each group in this study: 9 samples were used for the single-fiber pullout tests, while the remaining 3 samples were reserved for non-destructive microstructural analysis.

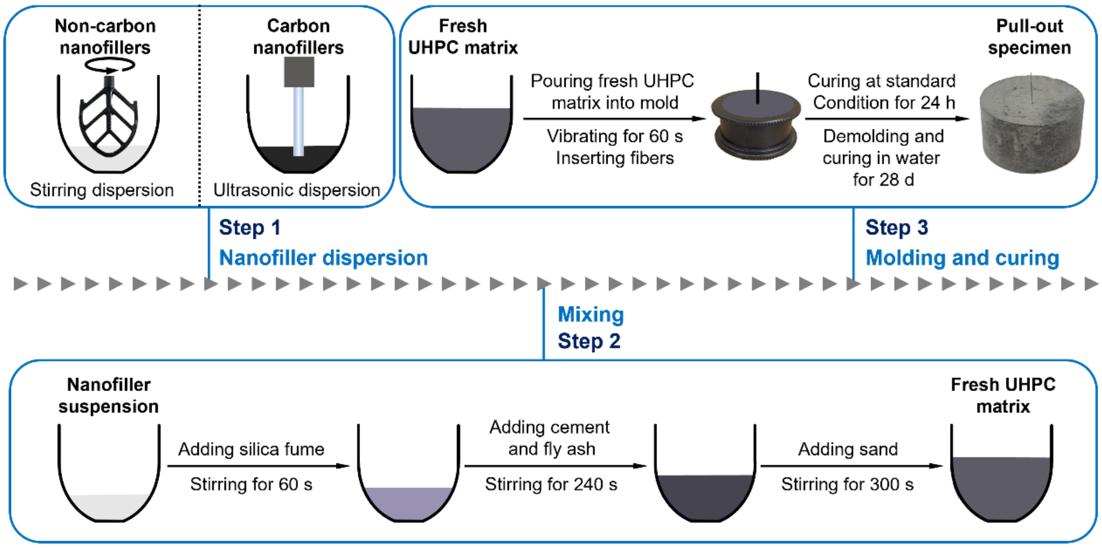

Fig. 1 Specimen preparation processes

2.2 Test setup

2.2.1 Interfacial Bond Evaluation

The bond behavior between steel fibers and UHPC matrix was characterized through single-fiber pull-out tests. A structural adhesive was used to bond the base of the cylindrical UHPC specimen to a fixed support. A uniaxial load was applied monotonically at a loading rate of 0.5 mm/min [44]. The pull-out force and displacement were recorded by the testing system. It is noteworthy that due to the minimal elastic deformation of both the steel fiber and the UHPC matrix, the recorded displacement was considered equivalent to the slip between the steel fiber and the UHPC matrix.

The maximum fiber stress ($\sigma_{\max}$) was used to reflect the stress state at the pull out failure of the steel fiber and is calculated according to Equation 3.

$$\sigma_{f,\max} = \frac{4P_{\max}}{\pi d_{\mathrm{f}}^2} \tag{3}$$

where $P_{\max}$ is the maximum pull-out load, and d_{f} (=0.2mm) represents the diameter of the steel fibers. The ultimate bond strength between the steel fiber and the UHPC matrix largely determines the composite performance of the steel fiber within UHPC.

The average bond strength (τ_{av}) can reflect the effect of steel fibers on crack resistance ability of UHPC [21]. It was calculated by using Equation 4. This equation assumes that the interfacial bond stress is uniformly distributed along the entire embedded length of the fiber.

$$\tau_{\mathrm{av}} = \frac{P_{\mathrm{max}}}{\pi d_{\mathrm{f}} L_{\mathrm{E}}} \tag{4}$$

where L_{E} (=4 mm) represents the embedded depth of the steel fibers.

The incorporation of steel fibers not only enhances the strength of concrete, but more importantly, improves the ductility of the material, effectively altering its brittle nature. Consequently, in addition to the average bond strength, the pull-out energy (W_{p}) was calculated using Equation 5 to reflect the energy dissipation capacity of steel fibers in UHPC.

$$W_{\mathrm{p}} = \int_{s=0}^{s=L_{\mathrm{E}}} P(s)\,\mathrm{d}s \tag{5}$$

where $P(s)$ and s represent the pull-out force and fiber slip, respectively. In addition to the pull-out energy, the equivalent bond strength (τ_{eq}) can serve as a direct parameter to indicate the strain-hardening behavior of UHPC reinforced with steel fibers [45]. In this study, the τ_{eq} was calculated using Equation 6, which assumes that the shear stress is uniformly distributed along the steel fiber.

$$\tau_{\mathrm{eq}} = \frac{2W_{\mathrm{P}}}{\pi d_{\mathrm{f}} L_{\mathrm{E}}^{2}} \tag{6}$$

2.2.2 Microstructural analysis

To investigate the modification mechanism of nanofillers on the bond behavior between steel fibers and UHPC matrix, SEM, BSE, and EDS characterizations were employed in this study. After the single-fiber pull-out test, the cylindrical UHPC matrix was split, and the interfacial morphology and element distribution were analyzed using SEM and EDS techniques, respectively. Noteworthily, the distribution of nanofillers within the UHPC matrix surrounding the fiber's normal direction is reflected by characterizing the distribution of specific elements, such as the element Ti in nano-TiO_2, the element Ni in Ni@CNTs, and the element N in nano-BN. Additionally, the pore distribution along the fiber normal direction was analyzed through BSE images combined with image processing methods [46]. As illustrated in Fig. 2 (a), the BSE images were first converted into grayscale images. Then, the cumulative curve of grayscale values was calculated based on the brightness histogram of the BSE image. Following Wong's method [47], a grayscale threshold for determining porosity was identified. Using this approach, image regions with grayscale values lower than the threshold were considered pores or cracks. Finally, wedge-shaped strips with a width of 1 μm were extracted from the BSE images within a 30 μm range from the steel fiber-UHPC matrix interface. The porosity (η) of the strip can be calculated using Equation 7.

$$\Phi_n = \frac{A_{n,\mathrm{pore}}}{A_{n,\mathrm{total}}} \tag{7}$$

where Φ_n represents the porosity of strip n, while $A_{n,\mathrm{pore}}$ and $A_{n,\mathrm{total}}$ denote the pore area and the total area of strip n, respectively. By combining multiple images, the entire steel fiber-UHPC matrix interfacial zone can be reconstructed, as shown in Fig. 2 (b). Subsequently, each BSE image was processed using the aforementioned method. Finally, the porosity at varying distances from the interface was determined. It is noteworthy that the final results for each group represent the average of observations from three undamaged fibers.

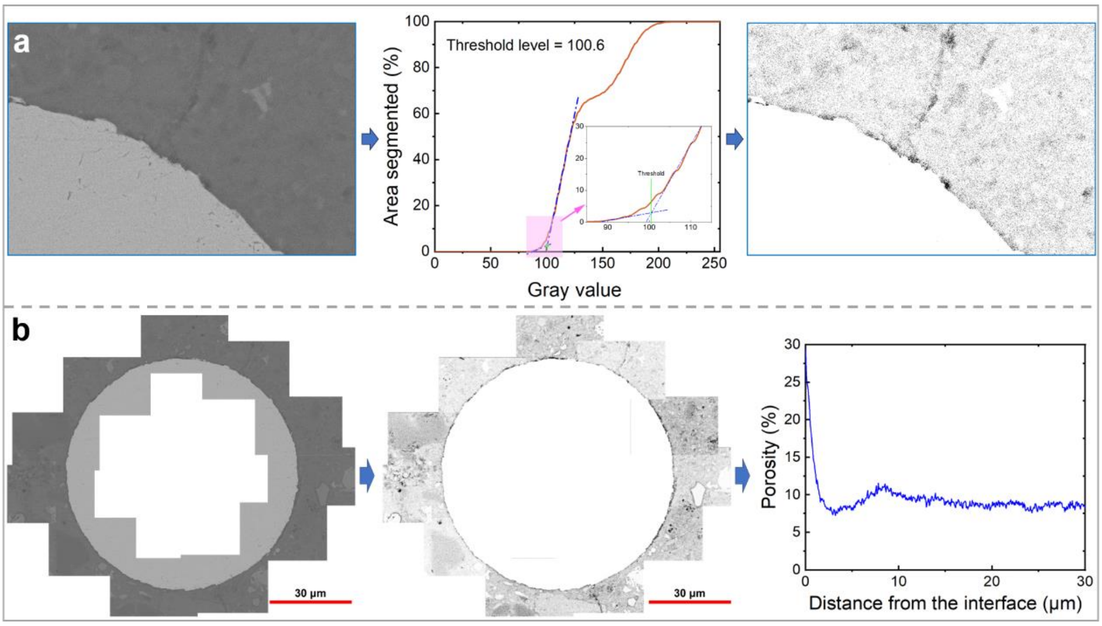

Fig. 2 Analysis method of pore distribution near steel fiber-UHPC matrix interface based on BSE images. (a) The judgment of pore region; (b) The method for obtaining the porosity at different distances from the interface

3 Result and discussion

3.1 Interfacial bond performance with nanofillers

Table 2 lists the characteristic parameters of the bond behaviors between steel fibers and the UHPC matrix, both with and without the inclusion of nanofillers. From Table 2, it can be observed that, in each group, the maximum fiber stress ($\sigma_{\max}$) is lower than the yield strength of the steel fiber (1100 MPa), indicating that all steel fibers were pulled out of the UHPC matrix. Thus, the measured pull-out force can be used to reflect the bond behaviors between the steel fibers and the UHPC matrix.

Fig. 3 shows a representative bond-slip curve in pull-out testing. As illustrated in Fig. 3, before the pull-out load reaches the initial cracking load (P_{ini}), there is a linear relationship between slip and pull-out load. This linear relationship between slip and pull-out load indicates that the applied load level is relatively low, thus preventing cracking in the interfacial transition zone. After the pull-out load exceeds P_{ini}, debonding gradually occurs between the steel fibers and the UHPC matrix. Then, the steel fibers become completely debonded from the UHPC matrix and begin to slip. In addition to the parameters described in Section 2.2.1, this study also uses P_{ini} to analyze the effect of nanofillers on the initial cracking threshold of the steel fiber-UHPC matrix interfacial bond. Since P_{ini} is influenced by the embedment length, the initial cracking shear strength (τ_{ini}=$P_{\mathrm{ini}}/(\pi d_{\mathrm{f}}^{2})$) was calculated in this study as well. As shown in Table 2, the presence of nanofillers can enhance the initial cracking bond strength, average bond strength, and equivalent bond strength of the interfacial bond between the steel fiber and UHPC matrix. The results indicate that incorporating 2 wt.% nano-TiO_2, 0.3 wt.% Ni@CNTs, and 0.5 wt.% MLG increases the initial cracking shear strength from 5.75 MPa to 7.81 MPa, 9.87 MPa, and 6.93 MPa, respectively, representing increases of 35.7%, 71.6%, and 20.6%. The improvement in initial cracking shear strength helps suppress crack formation in the steel fiber-UHPC matrix under load [48]. Moreover, the addition of nanofillers also enhances the average and equivalent bond strengths. With the incorporation of 3 wt.% nano-SiO_2, 0.3 wt.% H-CNTs, and 0.5 wt.% MLG, the average bond strength between steel fiber and UHPC matrix increases by 2.06 MPa/23.2%, 2.86 MPa/32.2%, and 0.76 MPa/8.6%, respectively. Similarly, with 3 wt.% nano-SiO_2, 0.3 wt.% Ni@CNTs, and 0.5 wt.% MLG, the equivalent bond strength reaches 12.88 MPa, 15.02 MPa, and 11.93 MPa, respectively, increased by 13.2%, 35.3%, and 4.8% compared to the control group. The improvements in average and equivalent bond strengths highlight the potential for enhancing the strength of steel fiber-reinforced UHPC [21]. Furthermore, the modification effect of one-dimensional (1-D) nanofillers on initial cracking shear strength is stronger than that of zero-dimensional (0-D) and two-dimensional (2-D) nanofillers.

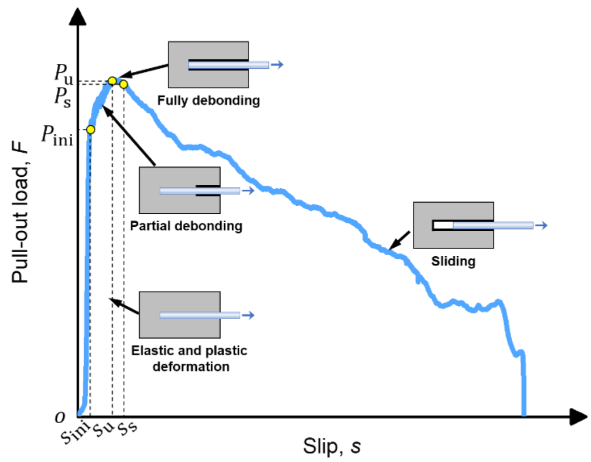

Fig. 3 Typical bond-slip curve between steel fiber and UHPC matrix

Table 2 Characteristic parameters of bond behaviors between steel fiber and UHPC matrix without/with nanofillers

Group	F_c (MPa)	$\sigma_{f,max}$ (MPa)	τ_{ini} (MPa)	τ_{av} (MPa)	τ_{eq} (MPa)	W_p ($\times10^{-3}$ J)
Blank	104.2	710.0	5.75	8.87	11.38	54.1
Nano-SiO_2	118.9	874.6	7.67	10.93	12.88	66.8
Nano-TiO_2	113.2	816.1	7.81	10.20	10.95	58.9
H-CNTs	130.5	938.2	8.15	11.73	15.02	76.6
Ni@CNTs	120.8	916.4	9.87	11.46	15.40	74.1
MLG	112.9	770.6	6.93	9.63	11.93	57.0
Nano-BN	104.6	763.7	6.90	9.55	11.70	57.8

The presence of nanofillers can also improve energy dissipation efficiency. As shown in Table 2, the pull-out energy absolutely/relatively increases by 12.7×10^{-3} J/23.5%, 22.5×10^{-3} J/41.6%, and 20.0×10^{-3} J/37.0% with the addition of 3 wt.% nano-SiO_2, 0.3 wt.% H-CNTs, and 0.3 wt.% Ni@CNTs, respectively. Meanwhile, the presence of nano-TiO_2, MLG, and nano-BN has a lesser impact on the pull-out energy. This phenomenon indicates that the size characteristics of nanofillers significantly influence the pull-out energy between the steel fiber and UHPC matrix, with 1-D nanofillers exhibiting an ideal modification effect.

In summary, the presence of nanofillers generally enhances the interfacial strength and energy dissipation capacity at the steel fiber-UHPC matrix, demonstrating significant potential for developing nano-engineered, high-strength, and high-toughness UHPC reinforced with steel fibers.

3.2 Microstructural characteristics

Fig. 4 illustrates the distribution of nanofillers within the UHPC matrix surrounding the fiber's normal direction by characterizing the distribution of specific elements, such as the element Ti in nano-TiO_2, the element Ni in Ni@CNTs, and the element N in nano-BN. It is evident that distribution patterns vary with nanofillers' dimensionalities. For 0-D nanofillers, a notable enrichment zone is observed in the interfacial transition zone. The formation of the zone attributes to the wall effect of fibers, i.e., the nanofiller particles with smaller sizes transfer toward fiber surface while binder particles with larger particles move away from the surface. This phenomenon is also observed in the cement paste-aggregate [31], cement mortar-aggregate [32], reinforcement-concrete [34, 35] interfaces. For 1-D nanofillers, the nanofiller content in the interfacial transition zone is similar to that within the UHPC matrix. Conversely, for 2-D nanofillers, the content at the interface is lower than that within the UHPC matrix. These phenomena can be attributed to similar particle sizes between steel fibers and binder particles. For the 1-D nanofillers, the surface of the steel fibers can still be regarded as a "wall", the tiny nanofiller particles accumulate towards the interface through the wall effect [49]. As the 1-D or 2-D nanofillers are on the micrometer scale in one or two dimensions, the steel fiber surface can no longer be considered as a "wall". Moreover, the passageways for migration through the gaps between binder particles toward the fiber surface are too small for 1-D and 2-D nanofillers. Therefore, the 0-D nanofillers still exhibit an interfacial enrichment effect, while the content of 1-D and 2-D nanofillers in the interfacial transition zone is similar to and lower than that in the UHPC matrix.

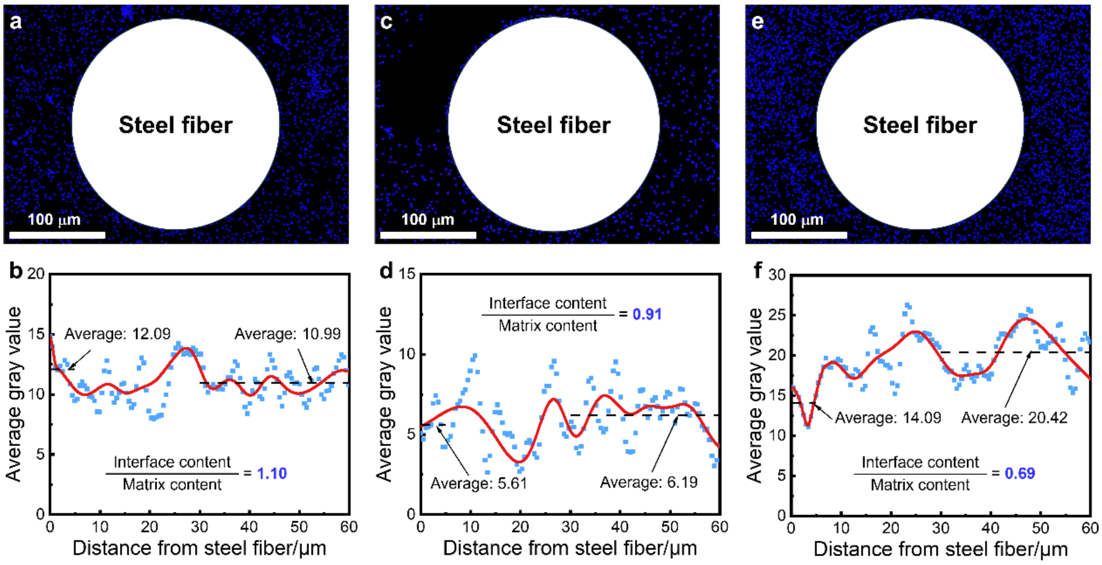

Fig. 4 Nanofiller distribution along steel fiber (a) and (b) Nano-TiO_2; (c) and (d) Ni@CNTs; (e) and (f) Nano-BN

Fig. 5 illustrates the microscopic morphology of steel fibers before and after pulled from UHPC matrix. As shown in Figs. 5 (a) and (b), the surface of steel fibers pulled from blank UHPC matrix appears smoother compared to that of unembedded fibers. Similarly, steel fibers pulled from the UHPC matrix containing nano-SiO_2 and nano-TiO_2 exhibit smooth surfaces, as shown in Figs. 5 (c) and (d). In contrast, steel fibers pulled from UHPC matrices incorporating H-CNTs, Ni@CNTs, MLG, and nano-BN, as depicted in Figs. 5 (e)-(h), show surface morphologies resembling those of unembedded fibers. These observations indicate that in blank UHPC, UHPC with nano-SiO_2, and UHPC nano-TiO_2, there is a weak zone near the surface of steel fibers, which is located within the UHPC matrix. Conversely, the damage appears to occur on the steel fiber surface, leaving the UHPC matrix near the fiber surface relatively intact, when UHPC contains H-CNTs, Ni@CNTs, MLG, and nano-BN. These phenomena indicate the presence of H-CNTs, Ni@CNTs, MLG, and nano-BN show strong improvement on the integrity of the transition zone near the fiber surface.

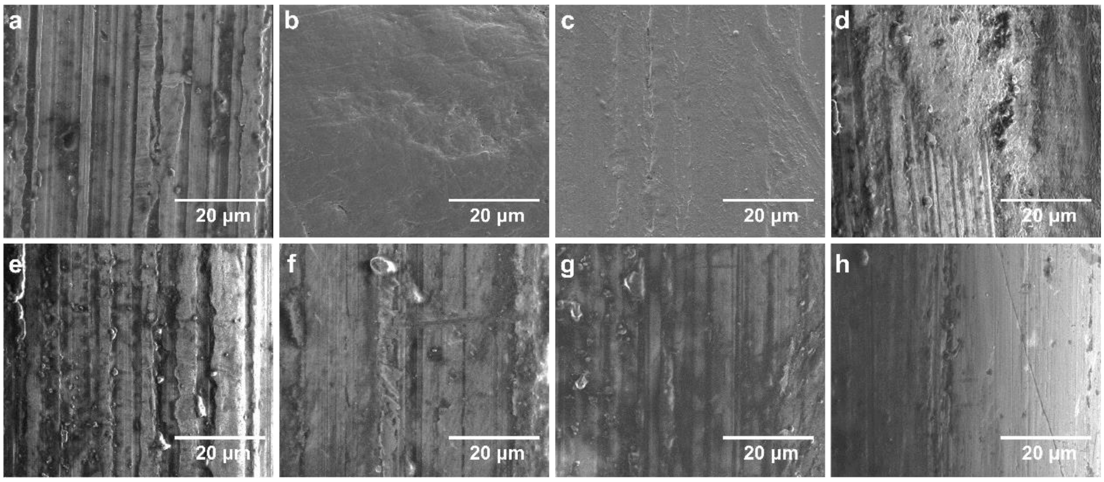

Fig. 5 Micromorphology (5000 ×) of (a) Unembedded fiber fibers and fibers pulled from (b) Blank UHPC matrix, (c) UHPC matrix with nano-SiO_2, (d) UHPC matrix with nano-TiO_2, (e) UHPC matrix with H-CNTs, (f) UHPC matrix with Ni@CNTs, (g) UHPC matrix with MLG, and (h) UHPC matrix with nano-BN

Fig. 6 shows the microstructure and CaO to SiO_2 (Ca/Si) ratio of the UHPC matrix at the fiber pull-out interface. As shown in Fig. 6 (a), the interface of blank UHPC matrix exhibits noticeable fish-scale-like cracks after fiber pull-out, indicating that the microstructure of the interface and the transition zone is damaged during the fiber pull-out process. After adding nanofillers, the cracks within the interface are significantly reduced, and the structure becomes denser, as shown in Figs. 6 (b)-(g). In particular, the presence of 1-D nanofillers (i.e., H-CNTs and Ni@CNTs) leads to numerous point-like protrusions appearing on the surface (Figs. 6 (d) and (e)). EDS analyses indicated that these protrusions are C-S-H gels. These point-like protrusions are likely formed by C-S-H gels growing from the tips of 1-D CNTs acting as nucleation sites [50]. The CNTs, being vertically distributed relative to the fibers, make the transition zone between steel fiber and UHPC matrix more intact. Additionally, these protrusions provide mechanical interlocking, resulting in higher bond strength. Furthermore, Fig. 6 (h) and Tables A1-A7 indicate that the Ca/Si ratio of the C-S-H gels in the interface of the UHPC matrix without nanofillers is 1.17. After the addition of nanofillers, the Ca/Si ratio at the interface decreases to 0.7-1.06. This indicates that the C-S-H structure becomes more silicified, forming more stable low-calcium C-S-H gels. At a low Ca/Si ratio, C-S-H gels tend to form a fibrous network structure, which exhibits higher mechanical properties [51]. In addition, C-S-H with a low Ca/Si ratio has a dense structure, which makes it more difficult for water molecules to penetrate the silicate chains, offering improved durability [52].

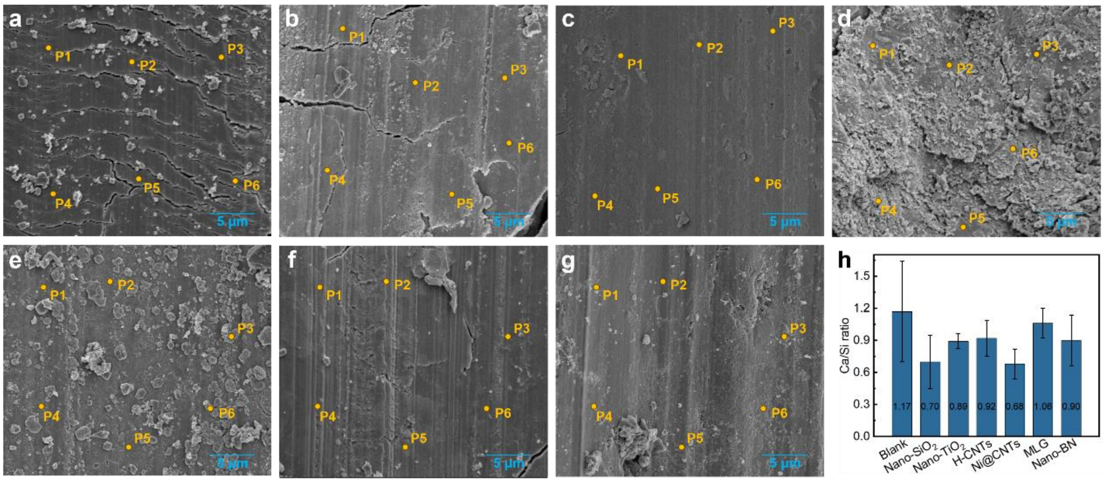

Fig. 6 Micromorphology of interface between steel fiber and (a) Blank UHPC matrix, (b) UHPC matrix with nano-SiO_2, (c) UHPC matrix with nano-TiO_2, (d) UHPC matrix with H-CNTs, (e) UHPC matrix with Ni@CNTs, (f) UHPC matrix with MLG, and (g) UHPC matrix with nano-BN; (h) Ca/Si ratio of UHPC matrix at the fiber pull-out interface

Fig. 7 presents the elemental distribution at different distances from the steel fibers in the UHPC matrix, oriented normally to the fibers. As shown in Fig. 7 (a), in the UHPC matrix without nanofillers, no significant enrichment of elements O, Al, Si, or Ca is observed. Additionally, some steel fiber fragments fell into these pores during polishing, resulting in a noticeable Fe accumulation zone around the fibers. This phenomenon indicates the porosity in transition zone near steel fiber surface is relatively high in the absence of nanofillers. When nano-SiO_2 is added, the elemental distribution pattern does not show significant changes, as shown in Fig. A1. In contrast,

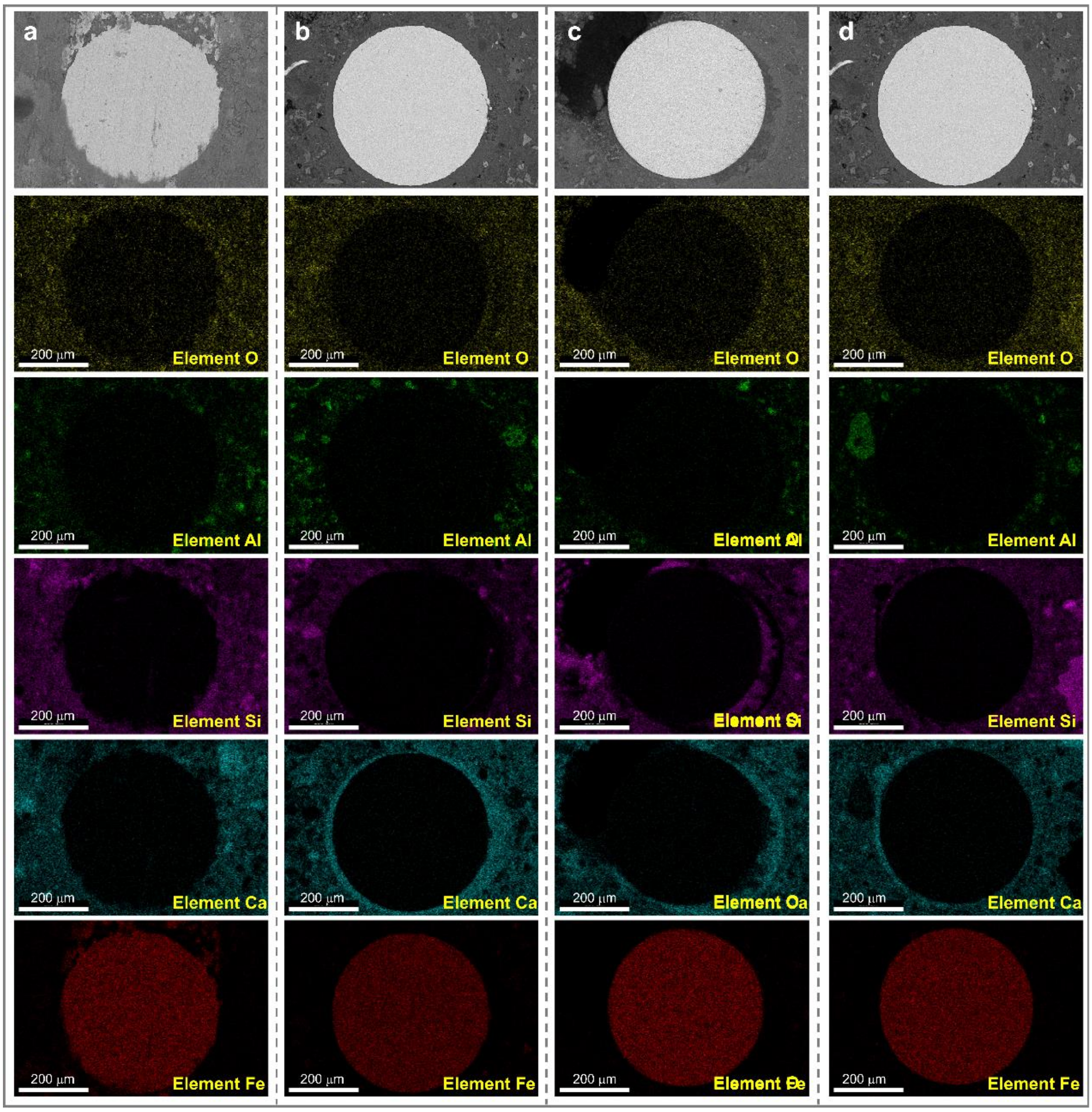

Fig. 7 Elemental distribution of the UHPC matrix along the fiber-normal direction: (a) Without nanofillers; (b) With nano-TiO_2; (c) With Ni@CNTs; (d) W ith MLG

as shown in Figs. 7 (b)-(d) and Figs. A2-A3, distinct Ca enrichment zones are observed at the steel fiber-UHPC matrix interfacial transition zone with the addition of nano-TiO_2, H-CNTs, Ni@CNTs, MLG, and nano-BN. This may be due to the negative charge on the surface of the nanofillers, which leads to the adsorption of a large number of metal cations (i.e., Ca^{2+}) on the surface of the steel fibers [53]. This also explains the decrease in the Ca/Si ratio in the C-S-H gels in Fig. 6, as a large amount of Ca^{2+} is adsorbed by the nanofillers and does not migrate further toward the steel fiber-UHPC matrix interface.

Fig. 8 shows the porosity at different distances from the steel fiber surface. It can be seen from Fig. 8 that the porosity at the steel fiber-blank UHPC matrix interface is 44.5%, while the porosity of the blank UHPC matrix itself is 14.0%. After the incorporation of nanofillers, the porosity at both the interface and the matrix significantly decreases. With the addition of nano-SiO_2, nano-TiO_2, H-CNTs, Ni@CNTs, MLG, and nano-BN, the porosity at the steel fiber-UHPC matrix interface decreases to 29.3%, 36.3%, 36.6%, 28.7%, 34.7%, and 20.5%, respectively; the porosity of the UHPC matrix decreases to 8.6%, 11.7%, 8.5%, 5.7%, 9.1%, and 9.6%, respectively. These changes in UHPC matrix porosity are consistent with previous work [54]. Additionally, the results show that the effect of nanofillers on the interface improvement does not always align with their effect on the UHPC matrix. For example, after the addition of Ni@CNTs, the porosity of the UHPC matrix decreases to 5.7%, but its improvement in interfacial porosity is relatively poor. Furthermore, the reduction in interfacial porosity is not always directly related to bond strength. As listed in Table 2, the addition of 1-D nanofillers significantly improves the bond performance between the steel fiber and UHPC matrix, but the improvement in the interfacial porosity is not the most optimal. Therefore, local bond performance may play a decisive role in the bonding strength, while the reduction in porosity (i.e., increased bonding area) does not dominate the enhancement of steel fiber-UHPC matrix bond performance.

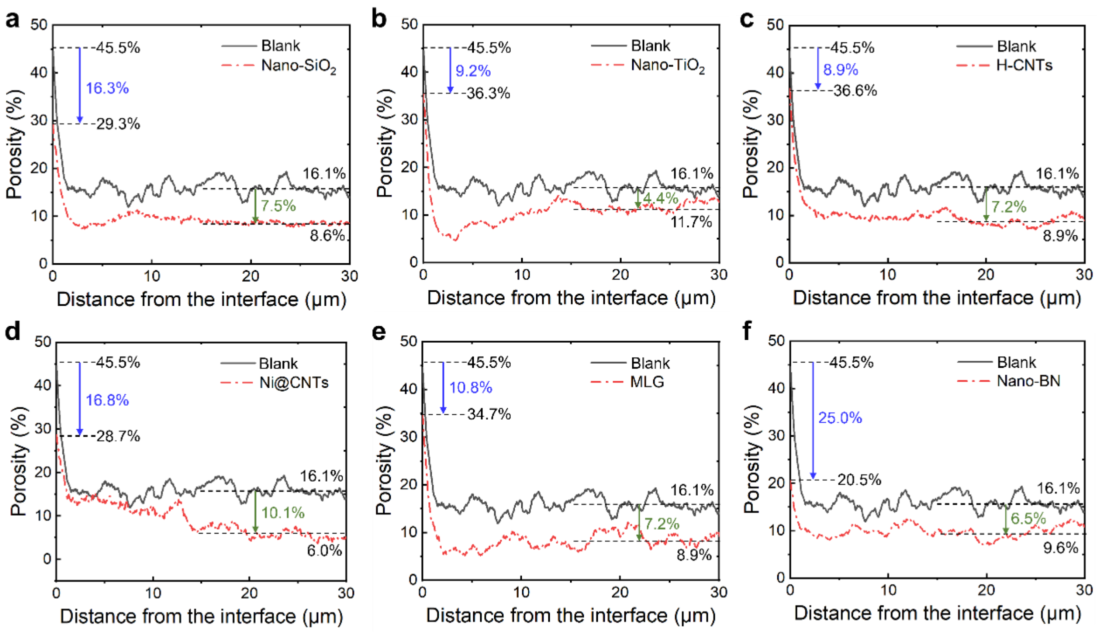

Fig. 8 Porosity of UHPC matrix at different distances from steel fibers (a) With nano-SiO_2; (b) With nano-TiO_2; (c) With H-CNTs; (d) With Ni@CNTs; (e) With MLG; (f) With nano-BN

Based on the above findings, the modification mechanisms of different nanofillers on the steel fiber-UHPC matrix interface are summarized as the interface nano-modification effect and the transition zone nano-modification effect, as depicted in Fig. 9. In the control group, the interface between steel fibers and UHPC matrix is loose with a high porosity. The C-S-H gels at the interface exhibit a high Ca/Si ratio. The transition zone near the fiber surface is also relatively loose, resulting in poor integrity. During the pull-out process, the failure surface is located within the transition zone, and some hydration products adhere to the fiber surface.

The effect of nanofillers in improving the interfacial bond behaviors is closely related to nanofillers physical dimensions, depending on whether the steel fiber is large enough to induce the wall effect. For 0-D nanofillers (e.g., nano-SiO_2 and nano-TiO_2), due to their tiny particle sizes, they can enrich in the steel fiber-UHPC matrix interface due to the wall effect [48]. The enriched nanofillers can act as nucleation sites to adhere Ca^{2+} ions and silicon oxygen tetrahedra, forming numerous nano-core-shell elements through nano-core effect [29]. The formation of nano-core-shell elements, on the one hand, prevents Ca^{2+} from migrating toward the interface, modifying the C-S-H gels in the interface by decreasing their Ca/Si ratio [52]. On the other hand, the elements contribute to reducing porosity in the interface and transition zone through the filling effect [54]. Owing to these modifications, the presence of 0-D nanofillers enhances the bond behaviors between steel fiber and UHPC matrix. However, due to the formation of nanofiller enrichment zone in the interface, the content of nanofillers within the transition zone near the fiber surface may be insufficient. As a result, the improvement effect of 0-D nanofillers on the fiber-concrete interface is superior to that in the transition zone near the fiber surface, indicating the improvement in bond performance primarily attributed to the interface nano-modification effect. The failure mode remains unchanged, with failure still occurring within the transition zone near the fiber surface. It should be noted that a densified interface does not always confer an advantage. On the one hand, the densified interfacial microstructure improves the initial and average bond strengths by reducing defects and limiting fragment generation during the pullout process. On the other hand, it decreases the bond ductility. In contrast, control specimens, where fractured UHPC fragments remain at the interface, benefit from enhanced mechanical interlocking. This additional interlocking increases the pullout energy and can result in a higher equivalent bond strength. Therefore, although nanofillers promote interfacial densification, the equivalent bond strength does not necessarily increase under all conditions.

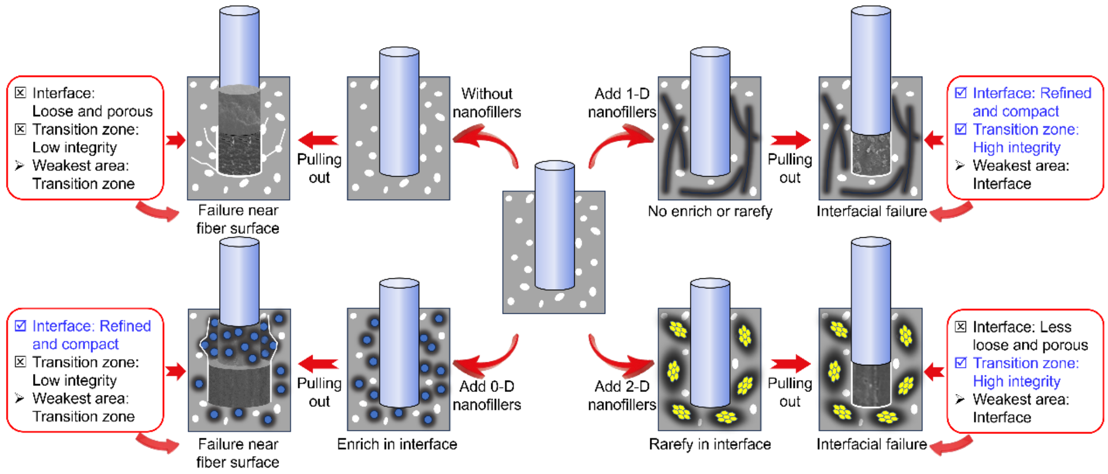

Fig. 9 The modification mechanisms of different nanofillers on steel fiber-UHPC matrix interface

In contrast, for 2-D nanofillers, due to their size being larger than that of small-particle binder materials (such as silica fume and fly ash), their density in the interface, under the wall effect, is lower than their density in the transition zone near the fiber surface, resulting in a nano-dilution zone in the interface. These 2-D nanofillers, distributed in the interfacial transition zone, can also serve as nucleation sites, exerting the nano-core effect to optimize hydration products and reduce porosity, similar to 0-D nanofillers [55]. Particularly, 2-D nanofillers can increase the integrity of the transition zone near the fiber surface through the bridging effect [56]. This helps maintain the structural integrity of the transition zone during the pull-out process, thereby improving the bond behaviors. However, the lack of sufficient nanofillers in the interface limits their ability to significantly improve the microstructure of the interface. The enhancement effect of 2-D nanofillers on the transition zone is more pronounced than on the steel fiber-UHPC matrix interface, with the enhancement in bond behavior primarily deriving from the transition zone nano-modification effect. After the composite with 2-D nanofillers, the fiber tends to be pulled out from the UHPC matrix along the fiber surface. Moreover, previous studies [57] have indicated that the layered structure of 2-D nanofillers can produce a lubricating effect, which may not be beneficial to the interfacial bond.

As for 1-D nanofillers, their diameter is still smaller than that of binder particles, but their length is greater than the diameter of binder particles. As a result, their distribution in the interface is roughly the same as that in the UHPC matrix, meaning there is no significant nanofiller-enrichment or nanofiller-dilution effect. These 1-D nanofillers can exert the interface nano-modification effect and the transition zone nano-modification effect at the same time, thereby showing the superior modification effect on the steel fiber-UHPC matrix interface. The improvement effect follows the order: 1D > 0D > 2D.

3.3 Local bond-slip constitutive relationship

The bond-slip curves obtained from the pull-out tests cannot directly provide the constitutive bond-slip relationship between the steel fiber and UHPC matrix, as the interfacial bond is not uniform along the entire embedded length of steel fiber. Intact bonding, partial damage, and slipping may occur simultaneously at different locations along the steel fiber-UHPC matrix interface. Therefore, this study employed the finite element method (FEM) combined with a cohesive-zone model to back-calculate the constitutive bond-slip relationship of steel fiber-UHPC matrix interface.

In this study, a FEM was developed using ABAQUS, where the size of steel fiber and its embedment depth are consistent with the experimental setup. To reduce computational costs while ensuring negligible boundary influence, the UHPC matrix diameter was set to 10 times the fiber diameter, following Saint-Venant's principle that boundary effects decay rapidly with distance. The geometric dimensions and mesh configuration are shown in Fig. 10 (a). Since there was no fracture in both steel fibers and UHPC matrix in the experiments, the fibers and matrix were considered as elastomers, as shown in Fig. 10 (b) and (c). The contact relationship between the steel fiber and UHPC matrix is crucial for the success of the simulation. The bond stress typically consists of three components: chemical bond, mechanical interlock, and frictional force. Among these, chemical bond exists only when the steel fiber-UHPC matrix interface is intact or slightly damaged, and it can be described using a cohesive-zone model from fracture mechanics, as shown in Fig. 10 (d). Mechanical interlock and frictional force, on the other hand, remain constant after relative displacement between the steel fiber and UHPC matrix occurs and can be described using a friction model, as depicted in Fig. 10 (e). However, traditional FEM platforms cannot simultaneously implement cohesive and friction models at the interface. Therefore, this paper adopts the method proposed by Alfano and Sacco [58], combining interfacial damage and friction in a cohesive-zone model. The shear stress $\tau_{\max}(\sigma)$ can be expressed as shown in Equation 8.

$$\tau_{\max}(\sigma)=\begin{cases}\tau_0 & \text{if } 0\geq\sigma>\dfrac{(\eta-1)\tau_0}{\mu}\\ \dfrac{1-D^*}{1-\eta D^*}\tau_0-\mu D^*\sigma & \text{if } \dfrac{(\eta-1)\tau_0}{\mu}\geq\sigma>\dfrac{\tau_0}{\mu(\eta-1)}\\ -\mu\sigma & \text{if } \sigma\leq\dfrac{\tau_0}{\mu(\eta-1)}\end{cases}\tag{8}$$

where τ_0 is a constant frictional bond stress that can be calculated from Equation 9. D^* reflects the damage corresponding to the maximum shear stress, as shown in Equation 10. σ represents the inner pressure between steel fiber and UHPC matrix. μ is the interfacial friction coefficient that can be calculated from Equation 9. η is a constant determined by the Mode I and Mode II fracture, with a value of 0.9 referring to previous work [58].

$$\tau_0=\frac{P_{\mathrm{b}}}{\pi d_f L_e}=\frac{\mu N}{\pi d_f L_e}\tag{9}$$

$$D^*=\frac{1}{\eta}\left(1-\sqrt{\frac{(1-\eta)\tau_0}{\mu|\sigma|}}\right)\tag{10}$$

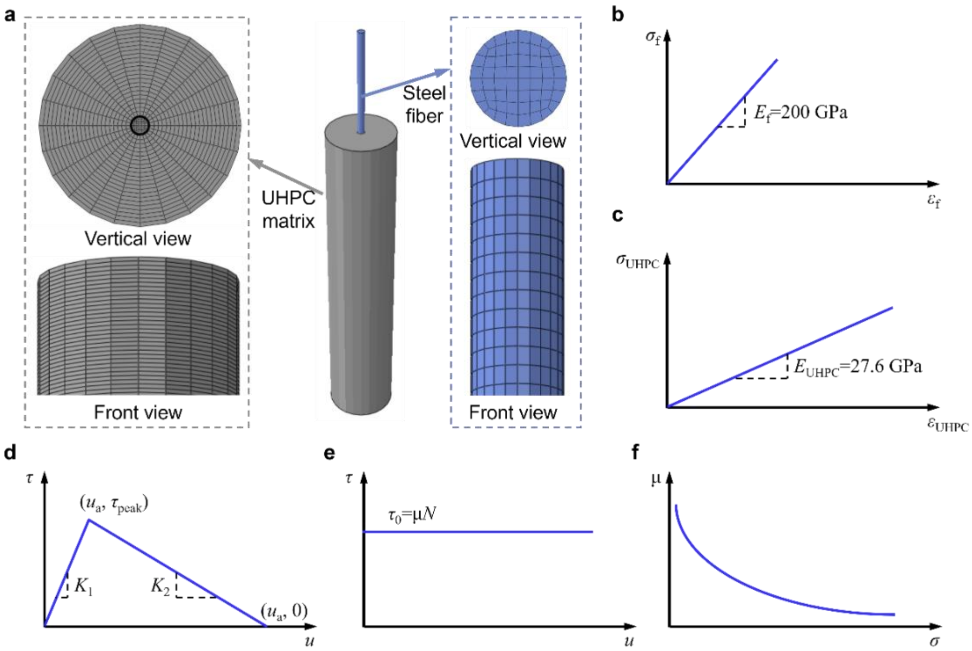

Fig. 10 Schematic of FEM simulation. (a) FEM model and grid division diagram; (b) Constitutive model of steel fiber; (c) Constitutive model of UHPC matrix; (d) Cohesive-zone model of steel fiber-UHPC matrix interface; (e) Friction model of steel fiber-UHPC matrix interface; (f) Constitutive model of steel fiber-UHPC matrix interface

In this way, chemical bonding, mechanical interlocking, and frictional forces can be incorporated into the FEM, as shown in Fig. 10 (f). The detailed derivation of the governing equations can be found in reference [59]. Apart from the tangential contact, the normal contact between steel fiber and UHPC matrix was set as hard contact in the model. Similar to the experiment, the bottom of the UHPC matrix cylinder was constrained; the steel fiber was pulled out from the UHPC matrix by using a displacement loading on the top of the fiber. It is worth noting that the curve shape often fluctuates greatly and has no obvious pattern in the late stage of the pull-out process, due to the complex microstructure damage and the very shallow fiber residual embedded depth. Therefore, only the first 2 mm pull-out force-displacement curve is compared between the simulation and experiment.

Fig. 11 presents a comparison between the experimental and FEM simulation results for each group. From Figs. 11 (a)-(g), it can be seen that the goodness of fit between the simulation and experimental results ranges from 0.762 to 0.910, suggesting that the simulation results accurately reflect the experimental results. Fig. 11 (h) shows that the shear stiffness between steel fiber and UHPC matrix significantly increases after incorporating composite nanofillers. The interfacial bond stiffness increases from 20.6/23.3 MPa/mm to 239.4/37.4 MPa/mm, 243.6/37.4 MPa/mm, 103.2/103.8 MPa/mm, 143.6/47.9 MPa/mm, 93.6/92.0 MPa/mm, and 44.1/56.4 MPa/mm, respectively, with the addition of nano-SiO_2, nano-TiO_2, H-CNTs, Ni@CNTs, MLG, and nano-BN. The increase in interfacial shear stiffness indicates that the composite nanofillers can significantly improve the interfacial microstructure [60]. Additionally, as shown in Fig. 11 (g), the presence of nanofillers generally decreases the coefficient of friction between steel fiber and UHPC matrix. The coefficient of friction decreases from 0.482 to 0.428, 0.420, 0.422, 0.412, and 0.455, respectively, after adding nano-SiO_2, nano-TiO_2, H-CNTs, MLG, and nano-BN. The low friction coefficient also indicates the low content of UHPC fragments in the interface. Meanwhile, the coefficient of friction increases to 0.552 with the incorporation of Ni@CNTs. The increase in the coefficient may derive from the increase in mechanical interlock due to the numerous point-like protrusions appearing on the surface, as shown in Fig. 6 (e). Based on the above results, it can be concluded that the use of nanofillers can enhance UHPC's crack resistance and effectively suppress crack propagation. Incorporating nanofillers into conventional UHPC has a positive effect on improving its mechanical strength and durability, but it may have an adverse effect on the ductility of UHPC.

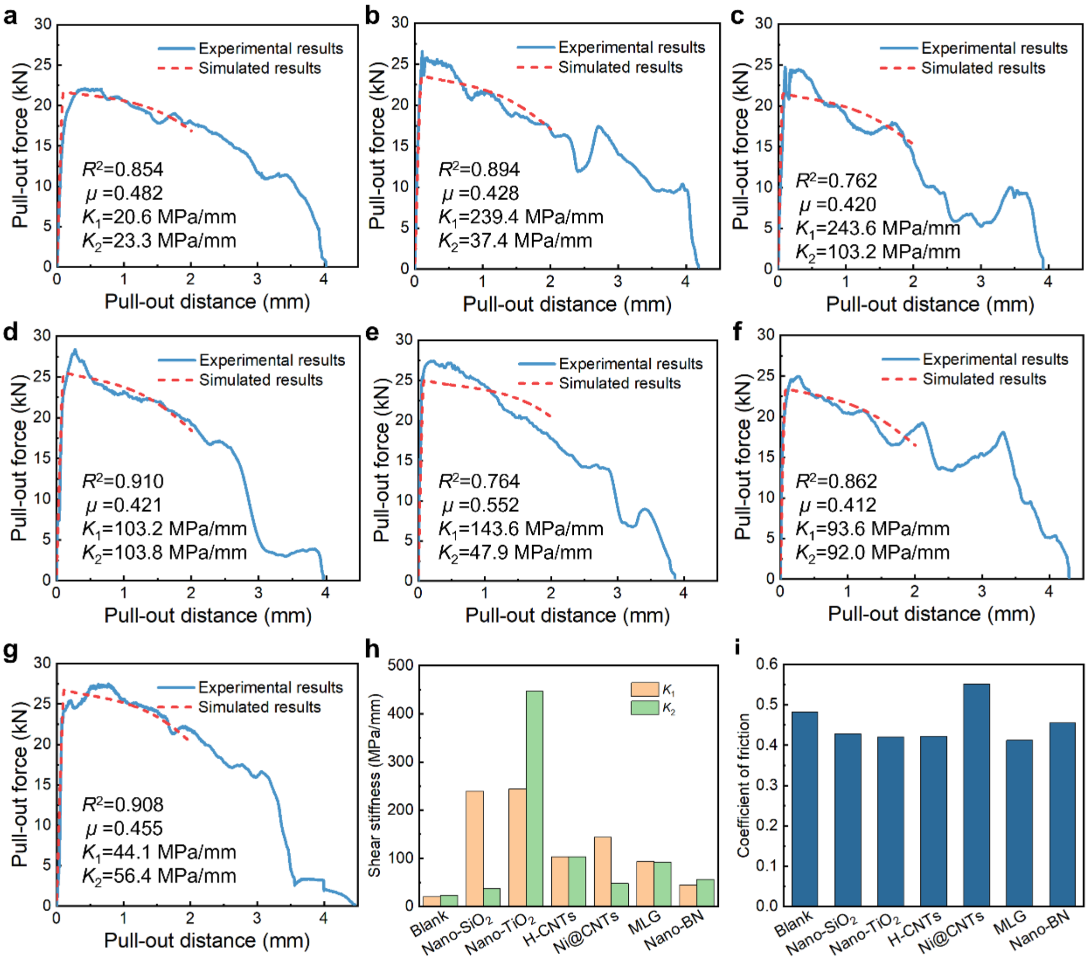

Fig. 11 Comparison between experimental and simulation results. The experimental and simulated bond-slip curve between steel fiber and UHPC matrix (a) Without nanofillers; (b) With nano-SiO_2, (c) With nano-TiO_2, (d) With H-CNTs, (e) With Ni@CNTs, (f) With MLG, and (g) With nano-BN; (h) The shear stiffness at steel fiber-UHPC matrix interface; (i) The coefficient of friction at steel fiber-UHPC matrix interface

4 Conclusion

This study investigated the local bond-slip behavior and underlying mechanisms at the interface between steel fibers and nano-engineered UHPC matrix, as well as established the local bond-slip constitutive relationship. The results indicated that the nano-engineering significantly improves the initial cracking shear strength, average bond strength, and equivalent bond strength at the steel fiber-UHPC matrix interface, with maximum improvements of 71.6%, 32.2%, and 35.3%, respectively. Moreover, nanofillers with different dimensionalities exhibit different distribution patterns at the steel fiber-UHPC matrix interface, depending on relative scale between nanofillers and steel fibers. 0-D and 2-D nanofillers show a respective enrichment and dilution effects at the interface due to the wall effect. While 1-D nanofillers have a similar concentration at the interface as in the UHPC matrix. The different distribution pattern leads to different modification mechanisms of various nanofillers. 0-D nanofillers strongly modify the steel fiber-UHPC interface by the filling effect of the nanofillers enriched in the interface, i.e., the interface nano-modification effect. 2-D nanofillers primarily enhance the transition zone near the fiber surface via improving interfacial integrity through the bridging effect in the transition zone, i.e. the transition zone nano-modification effect. 1-D nanofillers effectively improve both interface and transition zone between steel fiber and UHPC matrix, thereby exhibiting the superior modification effect on the bond behaviors. The addition of nanofillers significantly reduces porosity near the steel fiber-UHPC matrix interface, with SiO_2 lowering interfacial porosity from 44.5% to 29.3%. However, the reduction in porosity does not consistently correlate with the increase in bond strength, indicating that the local bond performance may play a decisive role in modifying bond behavior. Furthermore, the incorporation of nanofillers significantly enhances bond stiffness and crack resistance at the steel fiber-UHPC matrix interface, but decreases the coefficient of friction between steel fiber and UHPC matrix, indicating that while the incorporation of nanofillers into UHPC improves its mechanical strength and durability, it may simultaneously have an adverse effect on the ductility of UHPC. This work not only provides an efficient nano-technique to enhance the interfacial bond behavior between steel fibers and the UHPC matrix, but also reveals its underlying mechanisms from micro to macro levels, establishing a theoretical foundation for future design optimization and engineering application of nano-engineered UHPC.

Future studies should focus on developing advanced numerical models capable of capturing the complex interfacial behaviors, especially during the later stages of fiber pull-out process, where progressive matrix damage and residual embedded length dominate the response. In addition, this study only investigated the distribution and effects of nanofillers in the direction normal to the fiber surface. The spatial distribution of nanofillers along the fiber's tangential direction, as well as its influence on interfacial microstructure and bond performance, remains largely unexplored and warrants further investigation.

Acknowledgments

The authors thank the funding supported from the National Science Foundation of China (52308236, 52578268, and 52368031), the Major Science and Technology Research Project of the China Building Materials Federation (2023JBGS10-02), Natural Science Joint Foundation of Liaoning Province (2023-BSBA-077), and the Fundamental Research Funds for the Central Universities (DUT24GJ202).

Appendix

Table A1 Proportion of elements of interface between steel fiber and blank UHPC matrix

Position*	Element O	Element Al	Element Si	Element Ca	Ca/Si ratio
P1	52.74	2.03	16.53	28.71	1.74
P2	65.78	4.58	10.74	18.90	1.76
P3	57.59	2.67	19.84	19.90	1.00
P4	75.65	6.70	10.07	7.58	0.75
P5	71.74	2.86	12.29	13.11	1.07
P6	57.74	0.39	24.34	17.53	0.72
				Average	1.17

* The position refers to Fig. 7 (a)

Table A2 Proportion of elements of interface between steel fiber and blank UHPC matrix

Position*	Element O	Element Al	Element Si	Element Ca	Ca/Si ratio
P1	75.25	1.29	14.50	8.64	0.60
P2	69.32	2.39	17.13	10.27	0.60
P3	71.64	1.75	13.34	12.67	0.95
P4	73.63	2.25	15.35	7.36	0.48
P5	75.43	3.33	13.84	7.17	0.52
P6	56.85	1.78	19.25	20.66	1.07

				Average	0.70

* The position refers to Fig. 7 (b)

Table A3 Proportion of elements of interface between steel fiber and blank UHPC matrix

Position*	Element O	Element Al	Element Si	Element Ca	Ca/Si ratio
P1	80.37	3.25	7.83	7.08	0.90
P2	79.41	3.64	7.87	7.51	0.95
P3	80.52	3.37	7.58	7.25	0.96
P4	78.88	3.68	9.03	6.83	0.76
P5	79.85	2.98	8.19	7.45	0.91
P6	80.02	3.12	8.25	7.02	0.85
				Average	0.89

* The position refers to Fig. 7 (c)

Table A4 Proportion of elements of interface between steel fiber and blank UHPC matrix

Position*	Element O	Element Al	Element Si	Element Ca	Ca/Si ratio
P1	66.5	1.40	15.45	16.19	1.05
P2	54.78	1.86	20.55	21.86	1.06
P3	67.14	1.28	14.87	16.17	1.09
P4	68.28	1.70	15.39	14.03	0.91
P5	72.09	1.81	14.8	10.88	0.74
P6	61.93	3.84	19.82	13.79	0.70
				Average	0.92

* The position refers to Fig. 7 (d)

Table A5 Proportion of elements of interface between steel fiber and blank UHPC matrix

Position*	Element O	Element Al	Element Si	Element Ca	Ca/Si ratio
P1	56.26	2.43	20.48	14.86	0.73
P2	58.62	1.49	25.07	14.38	0.57
P3	73.27	3.10	14.52	8.70	0.60
P4	66.38	1.10	20.25	11.85	0.59
P5	59.28	1.34	20.03	18.77	0.94
P6	62.75	2.13	20.33	13.93	0.69
				Average	0.68

* The position refers to Fig. 7 (e)

Table A6 Proportion of elements of interface between steel fiber and blank UHPC matrix

Position*	Element O	Element Al	Element Si	Element Ca	Ca/Si ratio
P1	74.96	1.31	11.32	12.05	1.06
P2	77.2	1.17	9.98	11.29	1.13
P3	76.5	1.33	10.7	10.7	1.00
P4	78.6	1.04	10.7	9.42	0.88
P5	77.23	1.15	10.72	10.63	0.99
P6	80.6	1.04	7.35	9.41	1.28
				Average	1.06

* The position refers to Fig. 7 (f)

Table A7 Proportion of elements of interface between steel fiber and blank UHPC matrix

Position*	Element O	Element Al	Element Si	Element Ca	Ca/Si ratio
P1	80.77	1.15	8.04	8.71	1.08
P2	85.02	1.05	8.19	10.34	1.26
P3	79.27	1.48	10.31	6.97	0.68
P4	75.92	1.02	11.54	7.33	0.64
P5	86.91	1.08	8.56	7.8	0.91
P6	87.4	1.24	9.58	7.71	0.80
				Average	1.90

* The position refers to Fig. 7 (g)

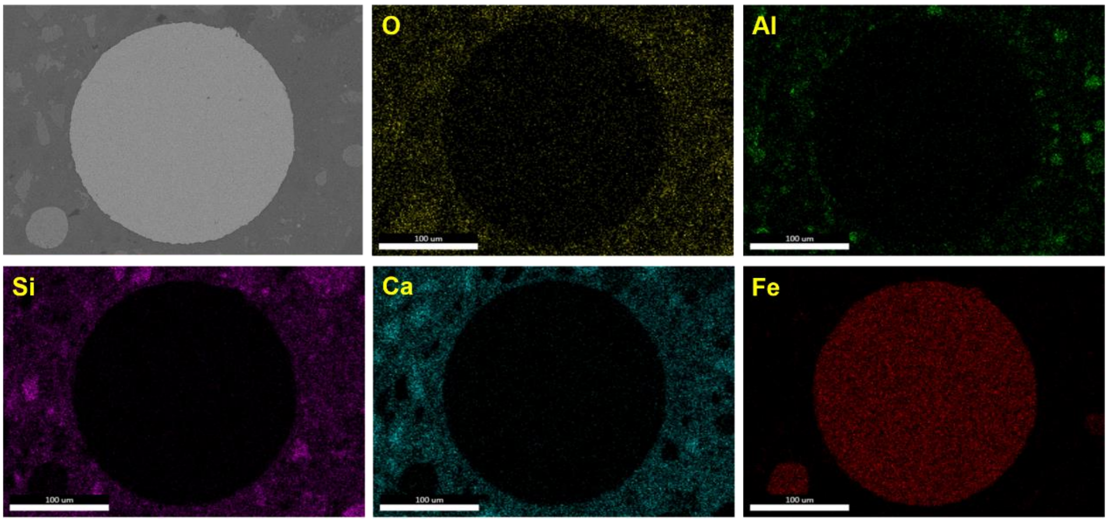

Fig. A1 Elemental distribution of the UHPC matrix with nano-SiO_2 along the fiber-normal direction

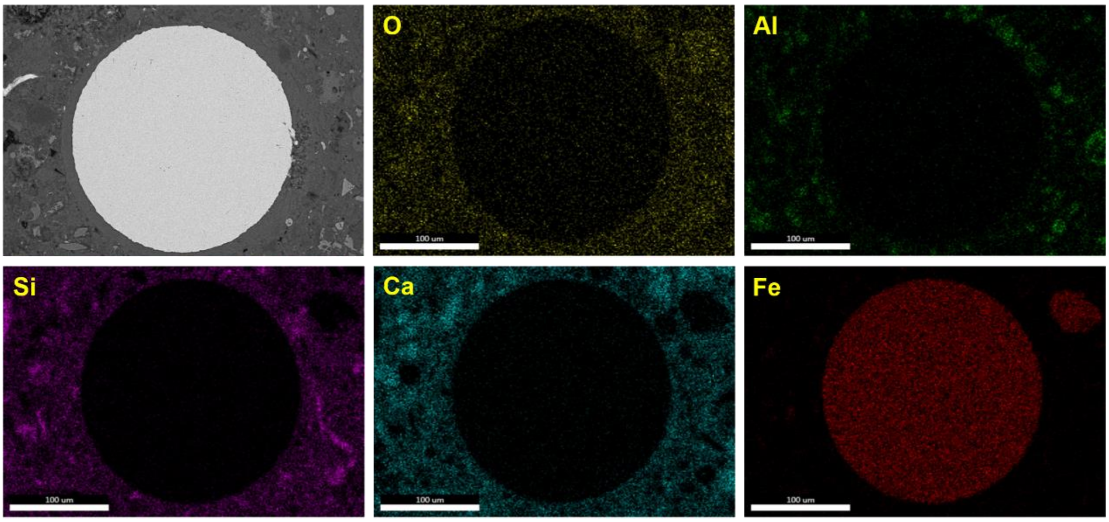

Fig. A2 Elemental distribution of the UHPC matrix with H-CNTs along the fiber-normal direction

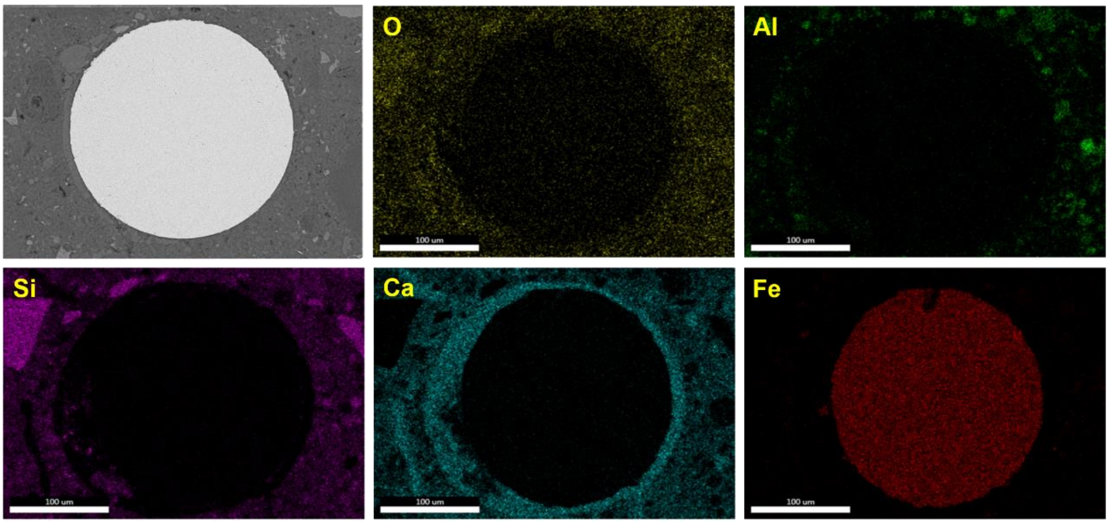

Fig. A2 Elemental distribution of the UHPC matrix with nano-BN along the fiber-normal direction

References

[1] B. Han, S. Ding, J. Wang, J. Ou. Nano-Engineered Cementitious Composites: Principles and Practices. Singapore: Springer, 2019.

[2] S. Mindess, J. F. Young, D. Darwin. Concrete. Sidney: Prentice Hall. 2002.

[3] P. K. Mehta, P. J. M. Monteiro. Concrete: Microstructure, Properties, and Materials. New York: McGraw Hill, 2013.

[4] C. C. Hung, H. S. Lee, S. N. Chan. Tension-stiffening effect in steel-reinforced UHPC composites: Constitutive model and effects of steel fibers, loading patterns, and rebar sizes. Composites Part B: Engineering. 2019, 158: 269-278. https://doi.org/10.1016/j.compositesb.2018.09.091

[5] Y. Chen, Y. Jiao, H. Yang, F. Ma, J. Meng. Interfacial bond behavior of steel fibers embedded in manufactured sand-based ultra-high performance concrete. Construction and Building Materials. 2024, 446: 138041. https://doi.org/10.1016/j.conbuildmat.2024.138041

[6] J. C. Maso. Interfacial transition zone in concrete. New York: E & FN Spon, 1996.

[7] Q. Chen, J. Zhang, Z. Wang, T. Zhao, Z. Wang. A review of the interfacial transition zones in concrete: Identification, physical characteristics, and mechanical properties. Engineering Fracture Mechanics. 2024, 300: 109979. https://doi.org/10.1016/j.engfracmech.2024.109979

[8] Z. Pi, Z. Wang, H. Xiao, J. Zhou, R. Liu. Tensile performance of cement-based composite reinforced with nano-SiO_2 modified steel fiber and its multiscale enhancement mechanism. Construction and Building Materials. 2025, 492: 143002.

[9] M. E. .E. Dandachy, M. Briffaut, F. Dufour. Experimental investigation of the transfer properties of ribbed and round steel rebars concrete interfaces under shear loading and after unloading. Construction and Building Materials. 2024, 451: 138746. https://doi.org/10.1016/j.conbuildmat.2024.138746

[10] S. Krishnaveni, S. Rajendran. Experimental studies on bond behaviour of steel rebar with different rib patterns in concrete. Journal of Building Engineering. 2024, 95: 110157. https://doi.org/10.1016/j.jobe.2024.110157

[11] E. D. Reis, R. C. de Azevedo, A. L. Christoforo, F. S. J. Poggiali, A. C. S. Bezerra. Bonding of steel bars in concrete: A systematic review of the literature. Structures. 2023, 49: 508-519.

https://doi.org/10.1016/j.istruc.2023.01.141

[12] E. P. Sumukh, S. K. Goudar, B. B. Das. A Review on the Properties of Steel-Concrete Interface and Characterization Methods. In: Shukla, S.K., Chandrasekaran, S., Das, B.B., Kolathayar, S. Smart Technologies for Sustainable Development. Lecture Notes in Civil Engineering, 2021, 78. Springer, Singapore. https://doi.org/10.1007/978-981-15-5001-0_15

[13] A.T. Horne, I. G. Richardson, R. M. D. Brydson. Quantitative analysis of the microstructure of interfaces in steel reinforced concrete. Cement and Concrete Research. 2007, 37(12): 1613-1623. https://doi.org/10.1016/j.cemconres.2007.08.026

[14] K. Turk, M. Karatas, Z. C. Ulucan. Effect of the use of different types and dosages of mineral additions on the bond strength of lap-spliced bars in self-compacting concrete. Materials and Structures. 2010, 43(4): 557-570. https://doi.org/10.1617/s11527-009-9511-1

[15] H. Shang, J. Zhou, G. Fan, G. Yang, W. You. Study on the bond behavior of steel bars embedded in concrete under the coupling of sustained loads and chloride ion erosion. Construction and Building Materials. 2021, 276: 121684. https://doi.org/10.1016/j.conbuildmat.2020.121684

[16] Z. Wu, K. H. Khayat, C. Shi. How do fiber shape and matrix composition affect fiber pullout behavior and flexural properties of UHPC. Cement and Concrete Composites. 2018, 90: 193-201. https://doi.org/10.1016/j.cemconcomp.2018.03.021

[17] S. Abdallah, M. Fan, K. Cashell. Pull-out behaviour of straight and hooked-end steel fibres under elevated temperatures. Cement and Concrete Research. 2017, 95: 132-140. http://dx.doi.org/10.1016/j.cemconres.2017.02.010

[18] D. Y. Yoo, N. Banthia, Y. S. Yoon. Recent development of innovative steel fibers for ultra-high-performance concrete (UHPC): A critical review. Cement and Concrete Composites. 2024, 145: 105359. https://doi.org/10.1016/j.cemconcomp.2023.105359

[19] D.Y. Yoo, M.J. Kim, S.W. Kim, J.J. Park. Development of cost effective ultra-high-performance fiber-reinforced concrete using single and hybrid steel fibers. Construction and Building Materials. 2017, 150: 383-394. https://doi.org/10.1016/j.conbuildmat.2017.06.018

[20] Y. Zhang, J.W. Ju, Q. Chen, Z. Yan, H. Zhu, Z. Jiang. Characterizing and analyzing the residual interfacial behavior of steel fibers embedded into cement-based matrices after exposure to high temperatures. Composites Part B: Engineering. 2020, 191: 107933. https://doi.org/10.1016/j.compositesb.2020.107933

[21] Y. Deng, Z. Zhang, C. Shi, Z. Wu, C. Zhang. Steel fiber-matrix interfacial bond in ultra-high performance concrete: A review. Engineering. 2023, 22: 215-232. https://doi.org/10.1016/j.eng.2021.11.019

[22] J. Yang, B. Chen, J. Su, G. Xu, D. Zhang, J. Zhou. Effects of fibers on the mechanical properties of UHPC: A review. Journal of Traffic and Transportation Engineering. 2022, 9(3): 363-387. https://doi.org/10.1016/j.jtte.2022.05.001

[23] J. Liu, F. Han, G. Cui, Q. Zhang, J. Lv, L. Zhang, Z. Yang. Combined effect of coarse aggregate and fiber on tensile behavior of ultra-high performance concrete. Construction and Building Materials. 2016, 121: 310-318. https://doi.org/10.1016/j.conbuildmat.2016.05.039

[24] D.Y. Yoo, S. Kim, J.J. Kim, B. Chun. An experimental study on pullout and tensile behavior of ultra-high-performance concrete reinforced with various steel fibers. Construction and Building Materials. 2019, 206: 46-61. https://doi.org/10.1016/j.conbuildmat.2019.02.058

[25] Z. Wu, C. Shi, K. H. Khayat. Influence of silica fume content on microstructure development and bond to steel fiber in ultra-high strength cement-based materials (UHSC). Cement and Concrete Composites. 2016, 71: 97-109. http://dx.doi.org/10.1016/j.cemconcomp.2016.05.005

[26] D. Y. Yoo, J. J. Park, S. W. Kim. Fiber pullout behavior of HPFRCC: Effects of matrix strength and fiber type. Composite Structures. 2017, 174: 263-276.

http://dx.doi.org/10.1016/j.compstruct.2017.04.064

[27] B. Han, S. Dong, J. Ou, C. Zhang, Y. Wang, X. Yu, S. Ding. Microstructure related mechanical behaviors of short-cut super-fine stainless wire reinforced reactive powder concrete. Materials & Design. 2016, 96: 16-26. https://doi.org/10.1016/j.matdes.2016.02.004

[28] J. J. Kim, D. Y. Yoo. Effects of fiber shape and distance on the pullout behavior of steel fibers embedded in ultra-high-performance concrete. Cement and Concrete Composites. 2019, 103: 213-223.

[29] B. Han, L. Zhang, S. Zeng, S. Dong, X. Yu, R. Yang, J. Ou. Nano-core effect in nano-engineered cementitious composites. Composites Part A: Applied Science and Manufacturing. 2017, 95: 100-109. https://doi.org/10.1016/j.compositesa.2017.01.008

[30] P. Shen, Y. Sun, S. Liu, Y. Jiang, H. Zheng, D. Xuan, J. Lu, C. S. Poon. Synthesis of amorphous nano-silica from recycled concrete fines by two-step wet carbonation. Cement and Concrete Research. 2021, 147: 106526. https://doi.org/10.1016/j.cemconres.2021.106526

[31] X. Wang, Q. Zheng, S. Dong, A. Ashour, B. Han. Interfacial characteristics of nano-engineered concrete composites. Construction and Building Materials. 2020, 259: 119803. https://doi.org/10.1016/j.conbuildmat.2020.119803

[32] X. Wang, S. Dong S, A. Ashour, W. Zhang, B. Han. Effect and mechanisms of nanomaterials on interface between aggregates and cement mortars. Construction and Building Materials. 2020, 240: 117942. https://doi.org/10.1016/j.conbuildmat.2019.117942

[33] X. Wang, S. Dong, A. Ashour, B. Han. Bond of nanoinclusions reinforced concrete with old concrete: strength, reinforcing mechanisms and prediction model. Construction and Building Materials. 2021, 283: 122741. https://doi.org/10.1016/j.conbuildmat.2021.122741

[34] X. Wang, S. Dong, A. Ashour, S. Ding, B. Han. Bond behaviors between nano-engineered concrete and steel bars. Construction and Building Materials. 2021, 299: 124261. https://doi.org/10.1016/j.conbuildmat.2021.124261

[35] X. Wang, S. Ding, L. Qiu, A. Ashour, Y. Wang, B. Han, J. Ou. Improving bond of fiber-reinforced polymer bars with concrete through incorporating nanomaterials. Composites Part B: Engineering. 2022, 239: 109960. https://doi.org/10.1016/j.compositesb.2022.109960

[36] Z. Wu. K. H. Khayat, C. Shi. Effect of nano-SiO2 particles and curing time on development of fiber-matrix bond properties and microstructure of ultra-high strength concrete. Cement and Concrete Research. 2017, 95: 247-256. https://doi.org/10.1016/j.cemconres.2017.02.031

[37] Z. Wu, K. H. Khayat, C. Shi, B. F. Tutikian, Q. Chen. Mechanisms underlying the strength enhancement of UHPC modified with nano-SiO2 and nano-CaCO3. Cement and Concrete Composites. 2021, 119: 103992. https://doi.org/10.1016/j.cemconcomp.2021.103992

[38] L. Yu, S. Bai, X. Guan. Effect of graphene oxide on microstructure and micromechanical property of ultra-high performance concrete. Cement and Concrete Composites. 2023, 138: 104964. https://doi.org/10.1016/j.cemconcomp.2023.104964

[39] X. Wang, D. Feng, X. Shi, J. Zhong. Carbon nanotubes do not provide strong seeding effect for the nucleation of C3S hydration. Materials and Structures. 2022, 55: 172. https://doi.org/10.1617/s11527-022-02008-5

[40] S. Bahl, A.K. Bagha. Finite element modeling and simulation of the fiber–matrix interface in fiber reinforced metal matrix composites. Materials Today: Proceedings. 2021, 39: 70-76. https://doi.org/10.1016/j.matpr.2020.06.160

[41] J. Esmaeili, K. Andalibi, O. Gencel, F.K. Maleki, V.A. Maleki. Pull-out and bond-slip performance of steel fibers with various ends shapes embedded in polymer-modified concrete. Construction and Building Materials. 2021, 271: 121531. https://doi.org/10.1016/j.conbuildmat.2020.121531

[42] China Standard CECS 13: 2009. Standard test methods for fiber reinforced concrete. 2009.

[43] X. Wang, S. Dong, L. Li, D. Wang, K. Zhang, Y. Wang, B. Han. Evaluating the effect of nanofillers on cement-based composites strength via artificial neural network and genetic algorithm. Materials Today Communications. 2023, 35: 105761. https://doi.org/10.1016/j.mtcomm.2023.105761

[44] Z. Wu, K. H. Khayat, C. Shi. Effect of nano-SiO2 particles and curing time on development of fiber-matrix bond properties and microstructure of ultra-high strength concrete. Cement and Concrete Research. 2017, 95: 247-256. https://doi.org/10.1016/j.cemconres.2017.02.031

[45] K. Wille, A. E. Naaman. Bond stress-slip behavior of steel fibers embedded in ultra high performance concrete. In: Mechtcherine V, Kaliske M, editors. Proc 18th European Conference on Fracture and Damage of Advanced Fiber-Reinforced Cement-Based Materials; 2010 Aug 29-Sep 3. p. 99-111.

[46] K. Lyu, W. She, C. Miao, H. Chang, Y. Gu. Quantitative characterization of pore morphology in hardened cement paste via SEM-BSE image analysis. Construction and Building Materials. 2019, 202: 589-602. https://doi.org/10.1016/j.conbuildmat.2019.01.055

[47] H. S. Wong, M. K. Head, N. R. Buenfeld. Pore segmentation of cement-based materials from backscattered electron images. Cement and Concrete Research. 2006, 36: 1083-1090. https://doi.org/10.1016/j.cemconres.2005.10.006

[48] M. Sharafisafa, Z. Aliabadia, L. Shen. Crack initiation and failure of block-in-matrix rocks under Brazilian test using digital image correlation. Theoretical and Applied Fracture Mechanics. 2020, 109: 102743. https://doi.org/10.1016/j.tafmec.2020.102743

[49] H. Chen, W. Sun, P. Stroeven. Interfacial transition zone between aggregate and paste in cementitious composites (I): Experimental techniques. Journal of the Chinese Ceramic Society. 2004, 32(1): 63-39.

[50] J. Wang, S. Dong, S. D. Pang, X. Yu, B. Han, J. Ou. Tailoring anti-impact properties of ultra-high performance concrete by incorporating functionalized carbon nanotubes. Engineering. 2022, 18: 232-245. https://doi.org/10.1016/j.eng.2021.04.030

[51] Y. Li, Z. Ding, X. Wang, X. Wang, B. Han. Molecular dynamics study on structural characteristics of amorphous C-S-H with different Ca/Si ratios. Journal of the American Ceramic Society. 2024, 108: 1-12. https://doi.org/10.1111/jace.20134

[52] D. Hou, H. Zheng, P. Wang, X. Wan, M. Wang, H. Wang. Molecular insight in the wetting behavior of nanoscale water droplet on CSH surface: Effects of Ca/Si ratio. Applied Surface Science. 2022, 587(4): 152811. https://doi.org/10.1016/j.apsusc.2022.152811

[53] X. Wang, S. Ding, A. Ashour, H. Ye, V. K. Thakur, L. Zhang, B. Han. Back to basics: Nanomodulating calcium silicate hydrate gels to mitigate CO2 footprint of concrete industry. Journal of Cleaner Production. 2023, 434(9): 139921. https://doi.org/10.1016/j.jclepro.2023.139921

[54] J. Wang, X. Wang, S. Ding, A. Ashour, F. Yu, X. Lv, B. Han. Micro-nano scale pore structure and fractal dimension of ultra-high performance cementitious composites modified with nanofillers. Cement and Concrete Composites. 2023, 141(4): 105129. https://doi.org/10.1016/j.cemconcomp.2023.105129

[55] X. Wang, S. Dong, Z. Li, B. Han, J. Ou. Nanomechanical characteristics of interfacial transition zone in nano-engineered concrete. Engineering. 2022, 17: 99-109. https://doi.org/10.1016/j.eng.2020.08.025

[56] H. Huang, L. Teng, X. Gao, K. H. Khayat, F. Wang, Z. Liu. Effect of carbon nanotube and graphite nanoplatelet on composition, structure, and nano-mechanical properties of C-S-H in UHPC. Cement and Concrete Research. 2022, 154: 106713. https://doi.org/10.1016/j.cemconres.2022.106713

[57] W. Zhang, B. Han, X. Yu, Y. Ruan, J. Ou. Nano boron nitride modified reactive powder concrete. Construction and Building Materials. 2018, 179: 186-197.

https://doi.org/10.1016/j.conbuildmat.2018.05.244

[58] G. Alfano, E. Sacco. Combining interface damage and friction in a cohesive-zone model. International Journal for Numerical Methods in Engineering. 2006, 68: 542-582. https://doi.org/10.1002/nme.1728

[59] B. Wu, P. Wang, J. Qiu. Autogenous healing of the interface between hollow natural fiber (HNF) and reactive magnesia cement (RMC) matrix. Construction and Building Materials. 2024, 422: 135843. https://doi.org/10.1016/j.conbuildmat.2024.135843

[60] Y. Su, J. Li, C. Wu, P. Wu, M. Tao, X. Li. Mesoscale study of steel fibre-reinforced ultra-high performance concrete under static and dynamic loads. Materials & Design. 2017, 116: 340-351. https://doi.org/10.1016/j.matdes.2016.12.027